Agricultural and Forest Meteorology 386 (2026) 111253

Contents lists available at ScienceDirect

Agricultural and Forest Meteorology

journal homepage: www.elsevier.com/locate/agrformet

Decoupling of greenness and photosynthesis regulates phenological shifts across Australian ecosystems

Jinru Xue [a,*], Luigi J. Renzullo [b], Alfredo Huete [a]

[a] School of Life Sciences, University of Technology Sydney, Sydney NSW 2007, Australia
[b] Bureau of Meteorology, Hydrology Science, Canberra, Australia

ARTICLE INFO

Keywords:
Greenness
Solar-induced chlorophyll fluorescence (SIF)
Drought
Land surface phenology
Vegetation structure
Vegetation function

ABSTRACT

The complex coupling between structural greenness and functional photosynthesis represents a critical interaction underlying uncertainties in the terrestrial carbon cycle. Greenness-based indicators, such as the leaf area index (LAI) and reflectance-derived indices, represent structural signals of canopy state but often fail to capture the spatiotemporal variations of photosynthetic function. In recent years, solar-induced chlorophyll fluorescence (SIF), as a direct remote-sensing proxy of photosynthesis, has provided a new avenue for exploring vegetation structure–function relationships. In this study, we treated SIF as a functional signal and greenness proxies as structural signals and examined when and where these signals were coupled (i.e., varied synchronously) or decoupled (i.e., differed in timing or magnitude) across Australia using multi-source remote sensing data. We then quantified the spatial variability of SIF–greenness coupling, assessed its associations with environmental and biological factors, and evaluated how variations in coupling accounted for discrepancies between structure- and function-based phenology. Our results indicated that the coupling between vegetation structure and function was primarily associated with vegetation composition and environmental aridity. In herbaceous ecosystems, low soil moisture (SMC) and high vapor pressure deficit (VPD) were linked to stronger coupling between greenness and photosynthesis. With increasing woody fraction (f_woody), the importance of SMC over VPD in influencing greenness–photosynthesis coupling became more pronounced. The relative roles of hydroclimatic and biological factors in greenness–photosynthesis coupling varied with the physical nature of each greenness indicator. Increasing decoupling between vegetation structure and function led to later peaks and shorter growing seasons in greenness-based phenology compared with SIF-based phenology, and these differences intensified with stronger decoupling. These findings advance the understanding of how environmental and biological factors are associated with vegetation structure–function coupling and its implications for phenology and carbon cycle modeling.

1. Introduction

Current terrestrial carbon cycle models primarily rely on greenness-based indicators, yet systematic biases can arise where vegetation structure and photosynthetic function are asynchronous, leading to substantial uncertainties in carbon cycle simulations (Badgley et al., 2017; Chang et al., 2019). Greenness, a structural trait of plants, has long been monitored from space by satellite systems via spectral indices or leaf area (Walther et al., 2016; Piao et al., 2019; Kong et al., 2020; Zhou et al., 2022). However, direct observation of photosynthesis, a functional trait, has until recent years been lacking (Walther et al., 2016; Li et al., 2023, 2019). While satellite-based monitoring of these plant traits has the advantage of large-area carbon cycle studies (Muraoka et al., 2013; Zhang et al., 2023a; Chen et al., 2022), there remains uncertainty in the exact relationship between greenness and photosynthesis, in particular the drivers of the coupling (or lack thereof) on regional (continental) scales (Hu et al., 2022).

The key assumption underpinning the coupling is that the greenness of the vegetation canopy (determined by leaf area and chlorophyll content) is temporally synchronized and coupled with the photosynthesis process (Kong et al., 2020; Zhou et al., 2022). However, this assumption often does not hold (Camps-Valls et al., 2021). For instance, under instant drought stress, there may be no noticeable variations in green biomass, while photosynthesis is already substantially reduced

* Corresponding author.
E-mail address: Jinru.Xue@uts.edu.au (J. Xue).

https://doi.org/10.1016/j.agrformet.2026.111253
Received 19 December 2025; Received in revised form 14 May 2026; Accepted 16 May 2026
0168-1923/© 2026 The Author(s). Published by Elsevier B.V. This is an open access article under the CC BY license (http://creativecommons.org/licenses/by/4.0/).

due to stomatal closure or declines in light use efficiency (Walther et al., 2016; Li et al., 2023, 2019). Also, in wet tropical forests, the decoupling may also arise from trade-offs between structural traits like leaf area index (LAI) and functional traits such as leaf photosynthetic efficiency (Hu et al., 2022). Asynchrony between greenness and photosynthesis can lead to substantial discrepancies between greenness-derived and photosynthesis-based phenology, reflecting differences in structural and functional responses to environmental drivers (Wu et al., 2017, 2016; Kong et al., 2020). When greenness changes synchronously with photosynthesis, phenological metrics derived from greenness indicators can reasonably reflect the dynamics of ecosystem carbon uptake. However, once decoupling occurs, these indicators may introduce systematic biases (Saleska et al., 2016; Hu et al., 2022; Chen et al., 2022). In comparison, photosynthesis-based phenology demonstrates greater environmental sensitivity because it reflects additional physiological regulatory mechanisms and functional variations that conventional greenness indices, which mainly track leaf pigment composition and canopy architecture, fail to capture (Zhang et al., 2016, 2020).

Solar-induced chlorophyll fluorescence (SIF) offers a new perspective for addressing this issue. It represents approximately 1–2% of the absorbed sunlight re-emitted by chlorophyll in the 640–850 nm spectral range during photosynthesis (Porcar-Castell et al., 2014). As a byproduct of photosynthesis, it is directly linked to photosynthetic carbon assimilation and reflects physiological photosynthetic processes (Gu et al., 2019; Liu et al., 2024). Compared with structural indices (e.g., LAI; normalized difference vegetation index, NDVI; and enhanced vegetation index, EVI), it can more sensitively capture changes in vegetation function and its responses to climate fluctuations (Guanter et al., 2014; Wang et al., 2020). Recent advances in satellite technology have made SIF a key tool for analyzing carbon and water flux dynamics across scales (Shan et al., 2021; Xue et al., 2024) and is increasingly being applied to track the seasonal dynamics of vegetation development (Zhang et al., 2022). Therefore, the coupling degree between vegetation greenness indices and SIF has itself become a diagnostic tool for assessing whether structural and functional dynamics are consistent.

In recent years, researchers have used temporal discrepancies between SIF and greenness to identify decoupling events (Hu et al., 2022). Furthermore, research has demonstrated the effectiveness of SIF in capturing the dynamics of true photosynthetic phenology (Zhang et al., 2023a). Quantifying the seasonal cycle of photosynthesis (i.e., phenology) across broad geographic scales is a central issue in climate change and global carbon cycle research (Richardson et al., 2013). Nevertheless, while previous studies have examined temporal differences between SIF- and greenness-based phenology mainly by comparing phenological metrics or describing their temporal trends, the influence of the degree of SIF–greenness coupling on discrepancies between greenness-based and SIF-based phenological metrics, such as the peak of season (POS) and length of season (LOS), remains insufficiently explored. Understanding this gap is critical to advancing the understanding and reliability of greenness-based phenology products.

Australian vegetation dynamics is often regarded as an indicator of climate change, as the continent's diverse ecosystems have evolved to be highly sensitive to rainfall and climate variation (Harris et al., 2018; Beringer et al., 2022). However, responses to climate variability and weather extremes differ substantially between ecosystems, and the synchronization between vegetation structure (e.g., greenness) and function (e.g., photosynthetic activity) at the continental scale remains insufficiently understood. In Australia, native deciduous trees and shrubs are scarce (Bennett et al., 2024), the primary woody cover consists of persistent foliage from plants with perennial leaves. In contrast, recurrent cover encompasses annual foliage, including both perennial and annual grasses as well as forbs (Donohue and Renzullo, 2025). This vegetation pattern implies that relying on LAI or reflectance-based greenness indices to assess the seasonal dynamics of ecosystem photosynthesis phenology in Australia may lead to misinterpretations of temporal carbon uptake patterns and their responses to climatic variability.

This study aims to reveal the coupling/decoupling patterns between vegetation photosynthesis and greenness in Australian ecosystems and to assess their associated uncertainties in remote sensing–based phenological parameter retrieval. We employed remote sensing datasets, including greenness proxies such as LAI, near-infrared reflectance of vegetation (NIRv), and total foliage cover (f_veg), as well as the photosynthesis proxy SIF. Together with environmental variables such as aridity index (AI), vapor pressure deficit (VPD), soil moisture content (SMC), and vegetation cover, we first analyzed the coupling/decoupling degree between SIF and three greenness indicators across Australia to reveal temporal discrepancies between vegetation photosynthetic and structural function. Next, the influence of biological and environmental factors on the degree of greenness–photosynthesis coupling across major Australian ecosystems was examined. Furthermore, we identified key phenological parameters for both photosynthetic phenology (derived from SIF) and greenness phenology (derived from greenness proxies). Finally, we examined how the degree of greenness-photosynthesis coupling ultimately regulates differences in key phenological metrics, such as the peak of season (POS) and the length of season (LOS).

2. Materials and methods

2.1. Flux-based GPP data

To examine the capacity of vegetation proxies to capture gross primary productivity (GPP) dynamics at flux tower sites, we obtained 12 sites within the OzFlux network (Beringer et al., 2022), which offer continuous measurements of carbon, water, and energy fluxes, as well as meteorological variables, based on the eddy covariance (EC) method. EC flux tower provide valuable in situ observations of the seasonal dynamics and interannual variations of net ecosystem exchange (NEE) between the land surface and the atmosphere (Baldocchi et al., 2001). NEE can be partitioned into its two main components: GPP, which represents the total net photosynthesis of all leaves at the ecosystem scale, and ecosystem respiration (ER). These measurements are also essential for evaluating satellite-derived vegetation products (Isaac et al., 2017). These 12 sites encompass the major vegetation types across different climatic zones in Australia and have updated data available after 2019. Among them, 6 sites are located in arid and semi-arid regions, while 6 sites are situated in tropical, subtropical, and temperate regions (Table 1). Of these, six sites are dominated by woody vegetation, whereas the other six are characterized by grasslands or open forest ecosystems.

2.2. TROPOMI SIF data

We used SIF observations from the Tropospheric Monitoring Instrument (TROPOMI) onboard the Sentinel-5 Precursor satellite (v2.1, L2B product) (Guanter et al., 2021). The L2B product provides both instantaneous and daily mean SIF values with global coverage at a spatial resolution of 7 km along track and 3.5–15 km across track (3.5 km at nadir). To minimize the influence of aerosols and clouds, only pixels with cloud fractions below 0.2 were retained. The SIF retrieval employed a data-driven approach within two spectral windows: 735–758 nm and 743–758 nm. We obtained daily mean ungridded TROPOMI SIF data for the period from 2019 to 2022, and, following the recommendation of Guanter et al. (2021), selected the "baseline" SIF product (743–758 nm). We aggregated the ungridded SIF data into a monthly $0.1^\circ \times 0.1^\circ$ gridded dataset by averaging all measurements within each grid cell based on the geographic locations recorded in the TROPOMI SIF observations.

2.3. MODIS satellite data

LAI data were obtained from MODIS Collection 6 MCD15A3H

Table 1
Summary of the 12 OZflux sites used in this study.

Site ID	Site name	Latitude (°)	Longitude (°)	Site description	Climate
AU-Cpr	Calperum	−34.0027°	140.5877°	Mallee woodland	Semi-arid
AU-Cum	Cumberland Plain	−33.6152°	150.7236°	Dry sclerophyll forest	Temperate
AU-Gin	Gingin	−31.3764°	115.7139°	Banksia woodland	Sub-tropical
AU-GWW	Great Western Woodlands	−30.1913°	120.6541°	Temperate Eucalypt woodland	Arid
AU-Wrr	Warra	−43.0950°	146.6545°	Eucalyptus obliqua forest	Temperate
AU-Wom	Wombat	−37.425°	144.094°	Dry eucalypt forest	Temperate
AU-Ync	Yanco	−34.9893°	146.2907°	Callitris glaucophylla	Semi-arid
AU-ASM	Alice Springs	−22.2828°	133.2493°	Acacia woodland & hummock grassland	Semi-arid
AU-DaS	Daly Uncleared	−14.1592°	131.3881°	Eucalypt open forest savanna	Tropical
AU-Dry	Dry River	−15.2588°	132.3706°	Open forest savanna	Semi-arid
AU-Lit	Litchfield	−13.1790°	130.7945°	Eucalypt open-forest savanna	Tropical
AU-Stp	Sturt Plains	−17.1507°	133.3502°	Mitchell grassland	Semi-arid

products (Myneni et al., 2015), which provide 4-day composite measurements at 500 m spatial resolution. These data were spatially aggregated to 0.1° grid cells to match the resolution of gridded SIF observations, and monthly mean LAI values were calculated for the period 2019–2022. NIRv was derived from the MODIS MOD09A1 surface reflectance product (Vermote, 2015) by multiplying NDVI (Myneni and Williams, 1994) with near-infrared reflectance, where NDVI is defined as the normalized difference between band 2 (near-infrared) and band 1 (red). NIRv was also resampled to 0.1° and summarized to monthly means. To ensure data quality, accompanying quality control flags were applied to exclude observations affected by cloud cover or elevated aerosol levels. Land use data was obtained based on the MODIS Land Cover (MCD12C1), which had a spatial resolution of 0.05° The spatial resolution of the land use data was rescaled from 0.05° to 0.1° using the nearest-neighbor method to match the SIF data.

2.4. Australian total foliage and woody foliage cover

We collected Australian total foliage (f_veg) and woody foliage cover (f_woody) data, which provide fractional estimates of green (live) foliage cover across Australia (Donohue and Renzullo, 2025), with separate delineations of woody and grass components. f_veg, equivalent to fractional vegetation cover, was derived from MOD13Q1, Collection 6.1, 250 m, 16-day NDVI composites (Didan et al., 2015) using the linear transformation proposed by (Carlson and Ripley, 1997). For arid regions, the transformation was parameterized by the minimum observed NDVI within the MODIS record, with a floor value of 0.2 imposed elsewhere. Woody and grass fractions were subsequently separated using version 3 of the persistent-recurrent splitting algorithm (Donohue and Renzullo, 2025), which fits f_woody as a curve to the annual minimum total cover time series, with grass cover defined as the residual. Validation against 4245 field observations from the Queensland SLATS Star Transects and OzFlux datasets indicates accuracies of 86–95% for woody vegetation types and 77–96% for treeless vegetation. The dataset is available as 16-day at 200 m spatial resolution covering continental Australia, with units expressed as fractions (0–1). We resampled the f_veg and f_woody to 0.1°× 0.1° grid resolution and aggregated to a monthly temporal resolution by calculating the arithmetic mean value.

2.5. Aridity index and climate data

The index of environment aridity was collected from the Global Aridity Index (Global-AI) datasets (Zomer et al., 2022) provided in Version 3 of the Global Aridity Index and Potential Evapo-Transpiration (ET0) Database (Global-AI_PET_v3). Global-AI provides a global climatology at 30 arc-second (~1 km) resolution, designed to quantify atmospheric water supply relative to potential evapotranspiration demand. The index is calculated as the ratio of mean annual precipitation (MA-Pr) to mean annual reference evapotranspiration (MA-ET_o), following the United Nations Environmental Programme (UNEP) formulation: AI = MA-Pr / MA-ET. Higher values of AI represent more humid environments, whereas lower values indicate arid conditions.

Daily air temperature, dew point temperature, SMC, and shortwave radiation were downloaded from the European Centre for Medium Range Weather Forecasts Reanalysis 5 (ERA5) (Muñoz-Sabater et al., 2021) and aggregated to a monthly temporal resolution by calculating the arithmetic mean value. VPD was then computed as the difference between saturation vapor pressure at air temperature and actual vapor pressure derived from dew point temperature. Finally, the AI and climate variables were all resampled to a monthly 0.1° × 0.1° spatial grid using bilinear interpolation.

2.6. Plant diversity and canopy height

Plant species richness was obtained from the ensemble prediction dataset developed by Cai et al. (2023), which combines observational records with machine-learning and statistical extrapolation methods. Among the tested models, XGBoost showed the strongest predictive performance and robustness, and therefore the XGBoost-based plant diversity predictions were used in this study.

The canopy height (m) data used in this study was obtained from global canopy height products developed by Potapov et al. (2021) and Lang et al. (2022), both based on spaceborne GEDI (Global Ecosystem Dynamics Investigation, Dubayah et al., 2020) lidar observations. GEDI was launched in December 2018, measures the vertical structure of vegetation using lidar footprints of approximately 25 m in diameter. Both plant diversity and canopy height data were resampled to 0.1°× 0.1° grid resolution using bilinear interpolation. Spatial distribution of plant diversity and canopy height across Australia can be found in Fig. S3.

2.7. Analysis

Analysis of the linear regression between greenness proxies and SIF was conducted to quantify the coupling degree between vegetation structural properties and photosynthetic activity at monthly temporal scales. Specifically, we fitted the greenness proxies–SIF relationships using monthly mean values of greenness proxies (e.g., LAI, NIRv, f_veg) and SIF for each pixel. The regression was performed independently for each pixel using up to 48 monthly observations over the 2019–2022 period. Pixels with fewer than 10 valid observations were excluded from the analysis. The coefficient of determination (R^2) was used as coupling strength.

To characterize the effects of vegetation component (f_woody) and aridity on the coupling between greenness proxies and SIF, we applied a two-dimensional binning strategy. To be specific, f_woody and the AI were divided into percentile bins (10th, 20th, …, 90th percentiles). For each bin, we summarized R^2 of linear regressions between greenness proxies (LAI, NIRv, f_veg) and SIF at the pixel scale. The statistical significance within each bin was determined via two-tailed t-tests ($p < 0.05$) to evaluate whether the mean correlation differs from the overall mean across all bins. We then conducted the same workflow by

replacing f_woody and the AI with VPD and SMC to examine their joint control on greenness proxies–SIF coupling.

We applied ridge regression to evaluate the sensitivity of SIF and greenness proxies to meteorological and biological conditions. For each pixel and vegetation proxy, we first constructed a multiple linear regression model to isolate the individual effects of VPD, SMC, photosynthetically active radiation (PAR), and f_woody. This enabled us to isolate the relative contributions of each climatic factor to variations in vegetation proxies across space and vegetation types. The multiple linear regression can be expressed as:

$$y = \sum_{i=1}^{4} \gamma_i \cdot x_i + \beta t + \varepsilon \quad (1)$$

where γ is a vegetation indicator (SIF, LAI, NIRv, or f_veg),γ_i ($i = 1,2,3,4$) is the vegetation sensitivities to the four concurrent hydroclimatic and biological factors, VPD, SMC, PAR, and f_woody. The regressor t was introduced as an augment term to mitigate spurious regression arising from variable trends, offering a more robust alternative to explicit detrending when handling stochastic trend (Hoerl et al., 1975).

Equation (1) was then written in first-difference form to remove the constant and reduce low-frequency dependence. The four sensitivity parameters (γ_1, γ_2, γ_3, and γ_4) were estimated with ridge regression after standardizing the regressors and response (first differences scaled to zero mean and unit variance). Regression coefficients characterize the degree of change in the dependent variable corresponding to unit changes in standardized independent variables. Since standardization has been applied, these coefficients are unitless and can therefore be directly compared across different models and predictor variables. The application of ridge regression effectively reduces the variability of regression slopes, which is particularly advantageous when addressing multicollinearity issues among hydroclimatic factors (Jin et al., 2023). The ridge factor was selected based on the method described in (Hoerl et al., 1975), and was implemented using the script at https://se.mathworks.com/matlabcentral/fileexchange/121008-autoridge. The ridge parameter was determined using the Hoerl–Kennard–Baldwin (HKB) method (Hoerl et al., 1975), in which the ridge parameter was estimated based on the residual variance and the magnitude of regression coefficients from an initial ordinary least squares regression.

To examine which climatic factor's sensitivity difference most strongly modulates the coupling between greenness proxies and SIF, we conducted a standardized regression coefficient (β) analysis on the national scale. For each pixel, we extracted the sensitivity differences between vegetation proxies and SIF for four environmental and biological factors (VPD, SMC, PAR, and f_woody). These sensitivity differences ($\Delta\gamma$) were derived from ridge regression analyses between each proxy and the environmental/biological factors, where the regression coefficients represent the sensitivity of each variable to variations in hydroclimatic and biophysical conditions. Before the multiple linear regression analysis, all variables were normalized using z-score standardization to enable direct comparison. Then, separate standardized regression models were fitted for LAI–SIF, NIRv–SIF, and f_veg–SIF, and we reported β with 95% confidence intervals to rank the relative importance of VPD, SMC, PAR, and f_woody.

2.8. Phenological metrics retrieval

Phenological metrics were derived from climatological seasonal cycles built from the monthly SIF and greenness proxies (LAI, NIRv, f_veg) over 2019–2022. For each pixel, the values of each indicator were averaged by calendar month over 2019–2022 to obtain a 12-month climatology. The POS was defined as the month of the climatological maximum (i.e. the month for which the climatology reaches its maximum value in the LAI, NIRv, f_veg, and SIF annual cycle). The start (SOS) and end (EOS) of season were identified as the first crossings of the 20% amplitude threshold on the ascending (green-up) and descending (senescence) phases around POS, respectively. The LOS was calculated as EOS – SOS (months). Pixels with climatological amplitudes below the median of the amplitude distribution across all pixels in Australia were excluded to remove areas with weak seasonal variability.

3. Results

3.1. Capability of SIF and greenness proxies in capturing GPP variability at Australian flux sites

The cross-site analyses of monthly averaged SIF and LAI showed the strongest correlations with monthly GPP_{EC}, both with a R^2 of 0.69 (Fig. 1a, b). NIRv and f_veg exhibited weaker linear relationships with GPP_{EC}, with R^2 of 0.55 and 0.59, respectively (Fig. 1c, d), indicating lower explanatory power in capturing photosynthetic CO_2 assimilation variations.

At the individual site level, the SIF-based regressions reproduced the tower-derived GPP measures well at the majority of OzFlux sites (Fig. 1e, i). Specifically, SIF showed stronger correlations with GPP in dense forest and woodland ecosystems with high LAI or homogeneous canopy structures. At the woody sites, SIF explained from 58% to 88% of the variance in monthly GPP_{EC}, with a mean of 74% (Fig. 1e). In contrast, at the sparser canopy sites or more complex underlying surface compositions such as shrublands, savannas, and grasslands, the relationship between SIF and GPP_{EC} was generally weaker than that observed in woody sites, with SIF explaining between 47% and 78% of the variance in GPP_{EC}, with an average explanatory power of 59% (Fig. 1i).

In comparison, although LAI also explained 69% of the GPP_{EC} variance across all sites (Fig. 1b), its explanatory power was significantly reduced at woody dominated sites, with an average (across 'x' sites) of 44.3% and range from 28% to 68% (Fig. 1f). In shrublands, savannas, and grasslands sites, the explanatory power reached 57%, ranging from 17% to 79% (Fig. 1j). The reduced explanatory power of LAI in denser evergreen forests indicates its limited ability to capture GPP variations, as LAI remains high and relatively stable year-round. However, SIF, as a direct proxy for photosynthesis and vegetation productivity, can more sensitively capture seasonal variations in photosynthetic activity and environmental stress.

NIRv and f_veg also exhibited relatively low average explanatory power for GPP_{EC} variance at woody sites, accounting for 47.5% and 46.2%, respectively (Fig. 1g, h). Although at some individual sites (e.g., Daly Uncleared and Dry River), NIRv and f_veg showed high correlations with GPP_{EC}, with explanatory power reaching 73%−86% (Fig. 1g, h), an anomaly is observed at the Wombat site in which NIRv exhibited a negative correlation with GPP_{EC} (Fig. 1g), and a similar negative relationship is also observed between f_veg and GPP_{EC} at the same site (Fig. 1h). Such decoupling or even negative correlations between greenness and GPP_{EC} also occurred in non-woody sites. For instance, the R^2 between NIRv and GPP_{EC} at the Gingin site was only 0.06 (Fig. 1k), and f_veg and GPP_{EC} were completely decoupled at the Calperum (with a R^2 value of 0.01), with negative correlations observed at Gingin and Great Western Woodlands (Fig. 1l).

3.2. Spatial patterns of greenness-SIF correlations across Australian biomes

To clarify the spatial distribution of the relationship between vegetation greenness proxies and SIF across Australia, we analyzed the national-scale distribution of the R^2 between SIF and greenness proxies including LAI, NIRv, and f_veg (Fig. 2a–c). The spatial distribution of valid daily SIF observations is shown in Fig. S1. Results showed that in most regions across Australia, the three greenness proxies were positively correlated with SIF. This is particularly evident in the northern, eastern, and southwestern semi-arid regions, where R^2 values commonly exceed 0.6, indicating that variations in greenness can effectively

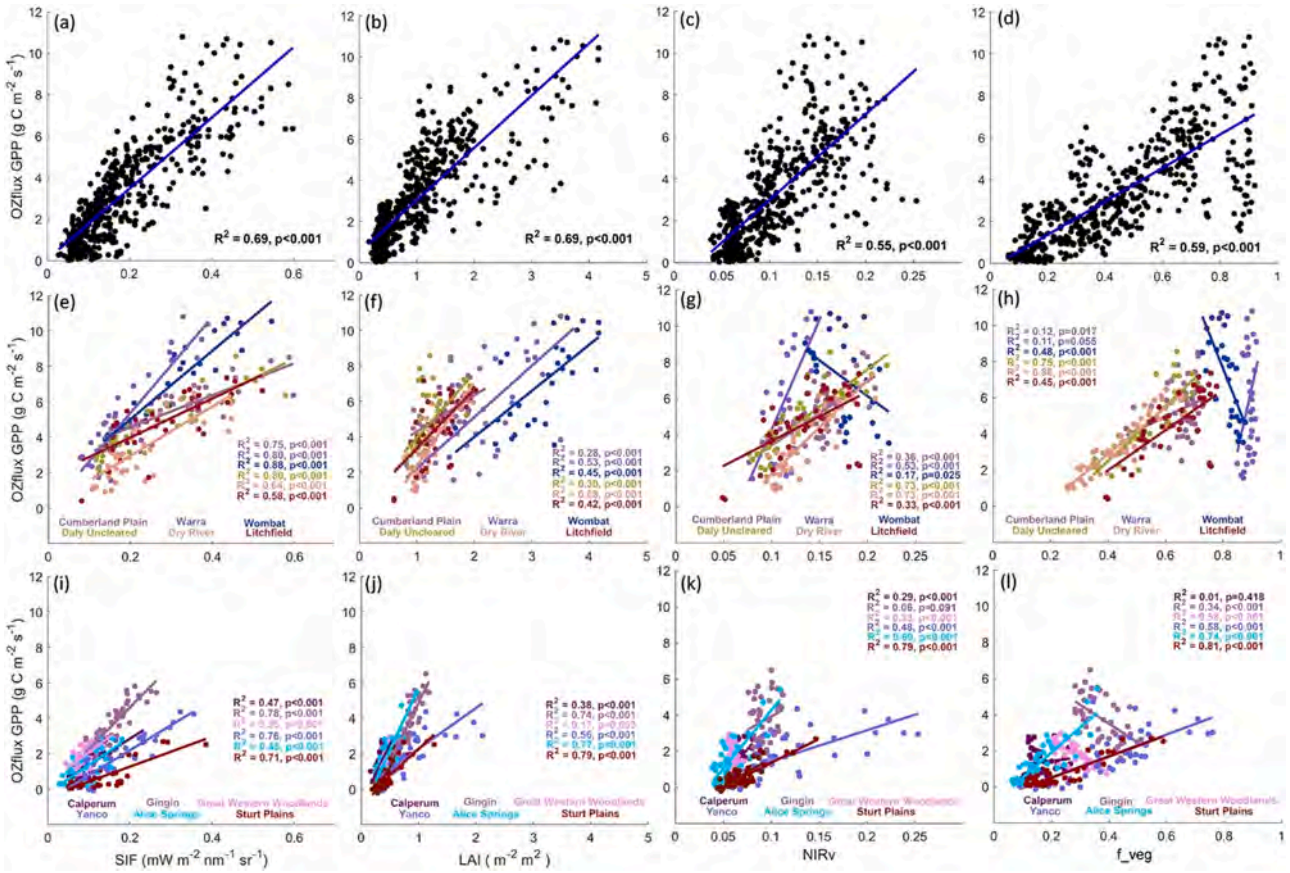

Fig. 1. Comparison between the monthly TROPOMI SIF (mW m^{-2} nm^{-1} sr^{-1}), MODIS LAI (m^{-2} m^2), MODIS NIRv, f_veg and GPP_{EC} (g C m^{-2} s^{-1}) for **(a)-(d)** all sites, **(e)-(h)** forest & woodland sites, and **(i)-(l)** shrub, savanna, and grass sites.

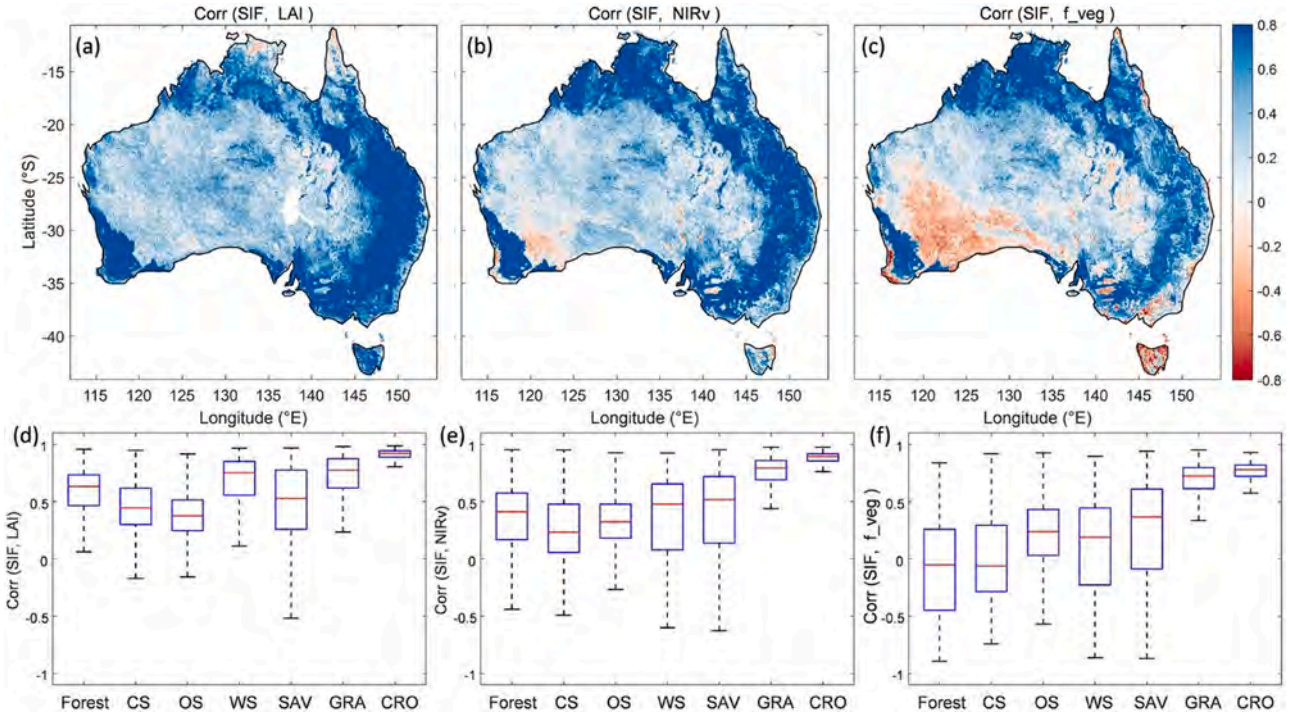

Fig. 2. Spatial patterns of correlations between SIF and three greenness proxies (LAI, NIRv, f_veg) across Australia, and their distribution across different ecosystem types. **(a–c)** Maps show the R^2 between SIF and **(a)**, LAI **(b)**, NIRv and **(c)** f_veg at a spatial resolution of 0.1° and monthly time scale. **(d–f)** Boxplots of R^2 between SIF and **(d)**, LAI **(e)**, NIRv and **(f)** f_veg for different ecosystem types. Boxplots indicate the median and interquartile range (IQR) for each ecosystem type, with whiskers extending to 1.5 × IQR. CS: closed shrubland; OH: open shrubland; WS: woody savanna; SAV: savanna; GRA: grassland; CRO: cropland.

represent the dynamics of vegetation photosynthetic function in these areas.

However, the SIF-greenness proxies relationship exhibited substantial spatial heterogeneity. In the arid regions of central Australia, greenness proxies were generally decoupled from SIF (Fig. 2a–c), with correlations approaching zero or even becoming negative, revealing a clear pattern of 'greenness-function decoupling'. Meanwhile, the decoupling phenomenon was also observed in humid areas across the northern, southeastern, southwestern, and Tasmanian coastal regions, where NIRv and f_veg also decoupled from SIF. In contrast, LAI maintained relatively strong coherence with SIF in most regions except the humid north, indicating a more stable structural relevance in a range of ecological contexts.

Boxplots of R^2 distributions (Fig. 2d–F) further illustrate the variability in SIF-greenness relationships across different ecological and background hydraulic conditions. In herbaceous ecosystems such as croplands (CRO) and grasslands (GRA), all three greenness proxies showed the highest correlation with SIF, indicating a tight synchrony between canopy structure and photosynthetic dynamics. In contrast, over woody ecosystems and mixed woody-herbaceous ecosystems (e.g., closed shrublands (CS), open shrublands (OS), woody savanna (WS), and savannas (SAV)) showed wider variation and lower median R^2 values, reflecting the difficulty of structural greenness proxies in capturing instantaneous photosynthetic changes in structurally complex environments.

Notably, R^2 between NIRv/f_veg and SIF exhibit an obvious structural gradient: R^2 increased progressively from woody ecosystems to structurally mixed woody-herbaceous systems (e.g., WS, SAV), and further to structurally simpler herbaceous ecosystems (e.g., GRA, CRO) (Fig. 2e, F). This pattern, which ranges from decoupling to coupling, highlights that the ability of structural greenness indicators to represent photosynthetic activity is strongly shaped by vegetation composition.

3.3. *Variations in greenness–SIF coupling across vegetation structure and hydroclimatic gradients*

We then analyzed the variations in correlations between different greenness proxies and SIF along a gradient of f_woody as well as a

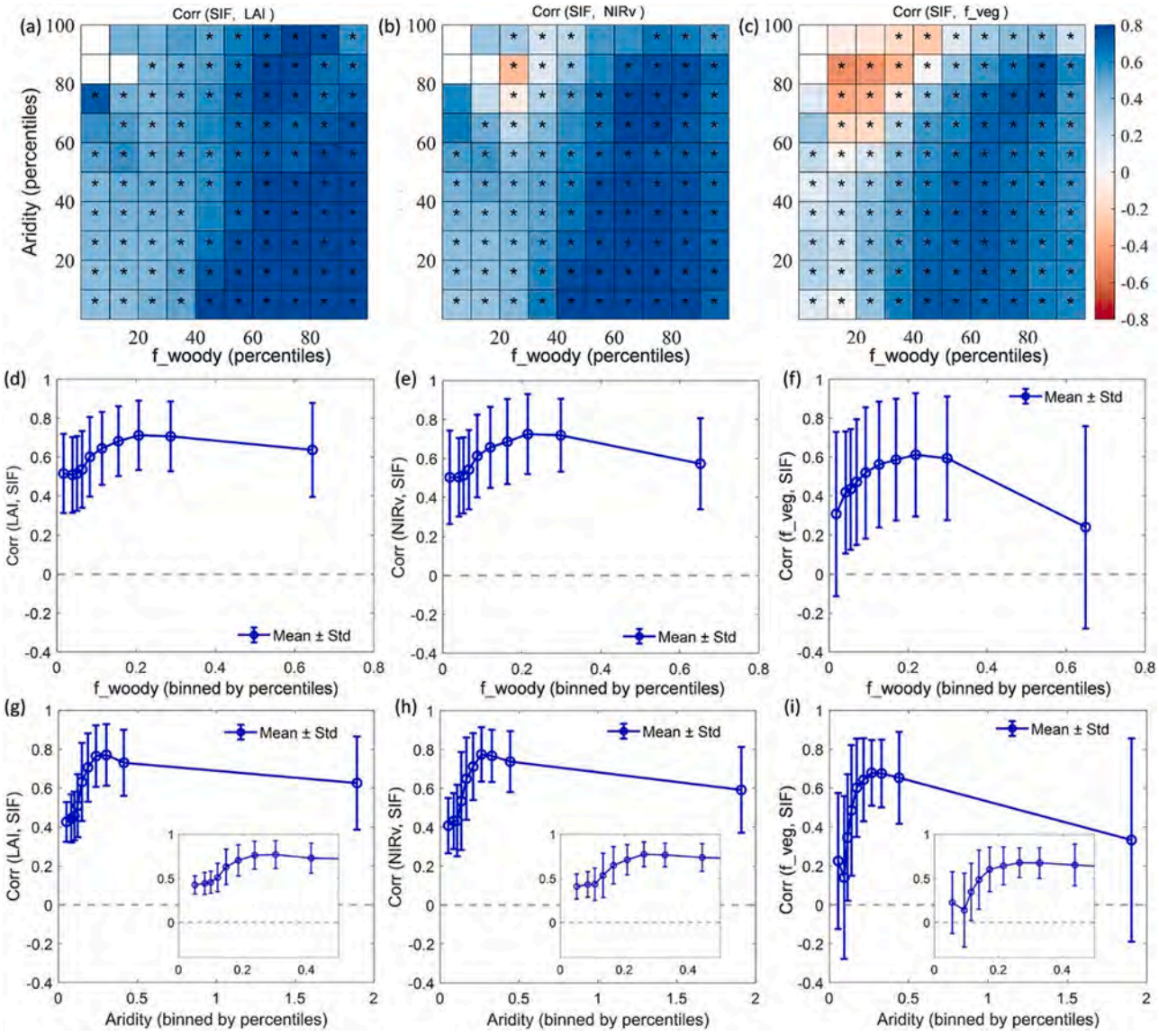

Fig. 3. Response of averaged correlations between SIF and **(a),** LAI; **(b)**, NIRv; **(c),** f_veg in each percentile bin of f_woody and aridity phase space. Panels (**d, e and f**) show the correlation gradients along f_woody, while panels **(g, h and i)** show the gradients along AI. The percentiles were the values of 10th, 20th, …, and 90th percentile of f_woody or aridity. '*' represents the correlations are significantly by t-tests ($p < 0.05$) across all areas for each bin. In **(d-i)**, blue solid lines represent the mean values for each bin, with error bars indicating standard deviation (std). Gray dashed lines indicate zero reference.

gradient of AI values (Fig. 3). The spatial distribution of aridity zones in Australia is shown in Fig. S2. As the f_woody fraction increases, the correlations between the three greenness proxies and SIF exhibited a rising-then-declining trend, with LAI showing relatively stable correlations (Fig. 3a, d). Both NIRv (Fig. 3b, e) and f_veg (Fig. 3c, F) showed pronounced declines in woody dominated ecosystems, with the decline being more pronounced for f_veg. This clarifying that the capacity of greenness proxies to capture photosynthetic activity weakens with increasing woody cover.

As a complement to the analysis based on f_woody, we also examined how the coupling between greenness proxies and SIF varies along the gradients of plant diversity and canopy height (m). Results showed that as plant diversity increases, the correlations between the three greenness proxies and SIF also exhibited a rising-then-declining pattern (Fig. S4a-c), which is consistent with the patterns observed along the f_woody gradient in Fig. 3d–F. This consistency can be explained by the tendency for ecosystems with a higher woody component to support greater plant species diversity. In addition, large areas of the arid interior of Australia are dominated by sparse vegetation with very low canopy height (< 1 m) and are therefore represented as zero height in the GEDI canopy height product (Fig. S3b). As canopy height increases along the arid–semi-arid transition, the correlations between greenness proxies and SIF strengthened. However, with further increases in vertical canopy structure and structural complexity, the coupling between greenness proxies and SIF weakened. These results provide additional evidence for the observed variations in SIF–greenness coupling.

In addition, the correlations between the three greenness proxies and SIF first increase rapidly and then decline gradually (Fig. 3g–i) along with the increasing AI. This suggests that increasing humidity generally strengthens the coupling between vegetation greenness and photosynthesis; however, in excessively humid regions, this relationship tends to decouple.

We further assessed the effects of dryness stress—characterized by VPD for atmospheric dryness and SMC for soil dryness—on the coupling between vegetation greenness indices and SIF. Photosynthetic activity is constrained by both soil water supply (e.g., SMC) and atmospheric drought stress (VPD), both of which exert independent and synergistic limitations on photosynthesis (Fu et al., 2022). To better characterize the underlying drivers of spatial heterogeneity in the relationship between SIF and greenness proxies, we introduced two key water stress variables (VPD and SMC) to evaluate their combined regulatory effects on the greenness-SIF relationship under varying climate conditions.

Our results demonstrated that, at the national scale, drought conditions characterized by high VPD (>70th percentile) and low SMC (<20th percentile) significantly strengthened the coupling between photosynthesis and vegetation structure (Fig. 4). In contrast, under more humid conditions (i.e., low VPD and high SMC), varying degrees of decoupling between greenness and SIF were observed. This indicated that under non-stress conditions, greenness indicators fail to capture short term fluctuations in photosynthetic activity, which leads to functional-structural decoupling. Moreover, both VPD and SMC exhibited strong effects on the LAI-SIF relationship (Fig. 4a), whereas VPD played a relatively more dominant role in shaping the correlations between SIF and NIRv/f_veg (Fig. 4b, c).

Given the observed variations in the greenness-SIF relationships across regions with varying vegetation composition (Fig. 3), we further conducted the analysis based on vegetation structural zones classified by f_woody (see Fig. S5 for vegetation structural zones), which represents a structural gradient from dense forested canopies to sparser herbaceous ecosystems. Within each woody composition zone, we examined how VPD and SMC jointly regulate the relationship between SIF and greenness proxies, and whether such regulation varies with climate background and vegetation structure (Fig. S6-8).

The effects of VPD and SMC on greenness–SIF coupling showed clear dependence on vegetation structure. The LAI–SIF relationship was predominantly positive across all regions (Fig. S6). In low woody fraction regions, LAI–SIF coupling strengthened markedly under low SMC and high VPD (Fig. S6a). Toward medium-to-high f_woody regions, the role of VPD diminished and soil water supply became the principal control, with moist soils leading LAI–SIF decoupling (Fig. S6b-d). NIRv–SIF exhibited a more pronounced structural dependence (Fig. S7). In herbaceous areas (Fig. S7a), coupling strengthened under low SMC and high VPD. At intermediate woody fraction, the influence of VPD weakened whereas SMC became the primary control; as SMC increased, NIRv–SIF tended to couple (Fig. S7b, c), suggesting that greater canopy closure made NIRv–SIF synchrony more vulnerable to soil drought. In forestry areas, NIRv–SIF was generally decoupled (Fig. S7d). The regulation of the f_veg–SIF relationship by VPD and SMC was similar to that of NIRv–SIF but showed the strongest structural dependence (Fig. S8): in low woody fraction areas (Fig. S8a), coupling degree increased significantly under low SMC and high VPD; with increasing canopy closure, SMC became the dominant control and soil water stress markedly induced f_veg–SIF decoupling (Fig. S8b-d).

Overall, in herbaceous ecosystems, low SMC and high VPD promoted greenness–photosynthesis coupling. As canopy closure increased, the relative importance progressively shifted toward SMC; under closed canopies, soil moisture stress more readily triggered decoupling of NIRv–SIF and f_veg–SIF, while tending to strengthen LAI–SIF coupling.

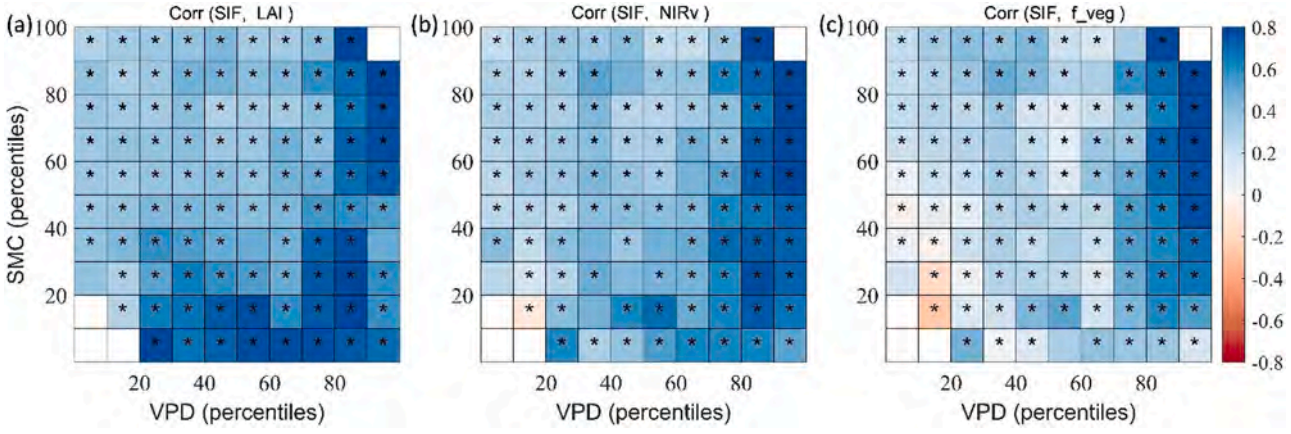

Fig. 4. Averaged correlation between **(a)**, LAI **(b)**, NIRv and **(c)** f_veg and SIF in each percentile bin of SMC and VPD phase space. The percentiles are the values of 10th, 20th, …, and 90th percentile of SMC or VPD. '*' represents the correlations are significantly by t-tests ($p < 0.05$) across all areas for each bin.

3.4. Sensitivities of vegetation greenness and photosynthesis to hydroclimatic and biological factors

Based on ridge regression, we quantified the hydroclimatic and biological controls on photosynthetic and greenness sensitivities across Australia (Fig. S9). Standardized regression coefficients (β) revealed the extent to which differences in the sensitivities ($\Delta\gamma$, ridge-derived sensitivity differences) of SIF and greenness proxies (LAI, NIRv, f_veg) to environmental (VPD, PAR, SMC) and biological factors (f_woody) modulate their coupling (Fig. 5). For importance ranking, we rank predictors by the absolute value of the β, larger |β| indicates a stronger influence.

For the LAI–SIF coupling (Fig. 5a), the sensitivity difference to f_woody exerted the largest effect (|β| = 0.447), followed closely by SMC (|β| = 0.422), whereas VPD and PAR showed weaker effect (|β| = 0.278 and 0.156, respectively), indicating that vegetation–water interactions and canopy composition strongly influence the structural–functional coupling. In the NIRv–SIF coupling (Fig. 5b), vegetation component–related constraints dominated, as indicated by f_woody (|β| = 0.449), whereas the contributions of hydroclimatic factors were relatively weak, with |β| values of 0.231, 0.256, and 0.179 for VPD, PAR, and SMC, respectively. For f_veg–SIF (Fig. 5c), PAR stood out as the dominant driver (|β| = 0.769), followed by VPD (|β| = 0.480). In contrast, f_woody (|β| = 0.398) and SMC (|β| = 0.230) showed weaker influences, indicating that radiation and atmospheric demand primarily controlled the coupling strength between f_veg and SIF.

3.5. Comparison of photosynthetic and greenness phenology and the effect of the coupling degree between SIF and greenness proxies on phenological differences

Following the analysis of SIF–greenness coupling and decoupling, we compared the photosynthetic and greenness phenology derived from SIF and greenness proxies across Australia. From 2019 to 2022, the spatial distributions of POS and LOS derived from SIF and greenness proxies across Australia are shown in Fig. 6. Overall, POS exhibited a clear latitudinal gradient (Fig. 6a, c, e, g): earlier POS generally occurred in the warmer northern tropical regions, where the POS derived from both SIF and greenness proxies typically appeared between January and April. With the shift in climate zones, the cooler southern temperate regions tend to reach their seasonal peaks between July and December. The interannual timing of POS also showed clear dynamics among different vegetation types. Specifically, in the cropping zones of NSW and WA, POS was earlier than in other vegetation types, usually between August and September, while forest POS tends to occur from November to January, and POS in savannas, grasslands, and shrublands in the north generally appears between February and April.

The LOS of photosynthetic phenology extracted from SIF was the shortest in cropping zones (Fig. 6b), usually lasting 3–4 months. LOS derived from LAI and NIRv exhibited a similar pattern (Fig. 6d, F), whereas f_veg produced a significantly longer LOS in cropping zones (Fig. 6h), lasting about 6–8 months. In southern forest regions, the photosynthetic LOS derived from SIF was generally 7–8 months (Fig. 6b), while the greenness LOS derived from LAI and NIRv was markedly longer (Fig. 6d, F). Notably, for phenology indicators derived from NIRv and f_veg, the weak seasonal variability in forested areas prevented the successful extraction of phenological metrics in some regions, with f_veg showing a more extensive missing area (Fig. 6f, h). In the remaining regions, the photosynthetic LOS extracted from SIF mainly ranged from 4 to 7 months, whereas the greenness-derived LOS was generally shorter. Fig. 7 further illustrates the spatial distribution of differences between greenness and photosynthetic phenological metrics during 2019–2022.

The coupling strength between vegetation greenness proxies and SIF significantly influences the temporal synchrony between photosynthetic and greenness phenological metrics (Fig. 8). For POS differences, our results showed that across different bins of SIF–greenness coupling, POS derived from greenness was generally later than POS derived from SIF (Fig. 8a, c, and e). Moreover, this difference gradually increased with weaker coupling, indicating that when photosynthetic activity and vegetation structural or optical responses are asynchronous, greenness-based indicators exhibit a systematic lag in capturing the POS of photosynthetic phenology. When the SIF–greenness correlation was relatively weak (e.g., SIF–greenness correlation < 0.4), POS derived from greenness lagged behind the photosynthetic POS by an average of 0.9–1.2 months. With increasing coupling strength, this temporal offset substantially diminished, and when the correlation exceeded 0.9, the two signals became nearly synchronized (POS differences ≈ 0 months).

In contrast, LOS differences exhibited opposite patterns (Fig. 8b, d, and F). Under weak coupling conditions (i.e., lower percentile bins of SIF–greenness correlation), LOS derived from greenness was about 0.9–1.8 months shorter than that derived from SIF. As coupling strength increased, LOS differences gradually decreased and even reversed in highly coupled regions. To be specific, for LAI, the LOS difference was about –1.5 months in decoupled areas, meaning that the LOS estimated by LAI was shorter than that from SIF by 1.5 months. However, with

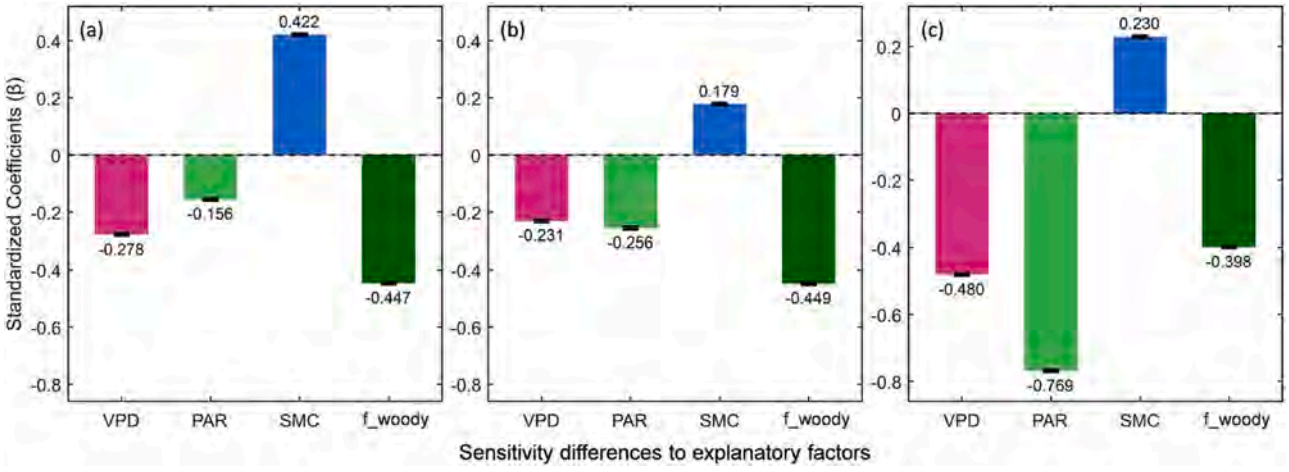

Fig. 5. Standardized regression coefficients (β) reveal how environmental and biological sensitivity differences between SIF and greenness proxies modulate their coupling relationships. Panels show the effects of sensitivity differences to factors on coupling degree for **(a)** LAI–SIF, where sensitivity difference = γLAI - γSIF for each factor, **(b)** NIRv–SIF, (γNIRv - γSIF), and **(c)** f_veg–SIF (γf_veg - γSIF). Environmental and biological factors include VPD, PAR, SMC, and f_woody. Error bars represent 95% confidence intervals.

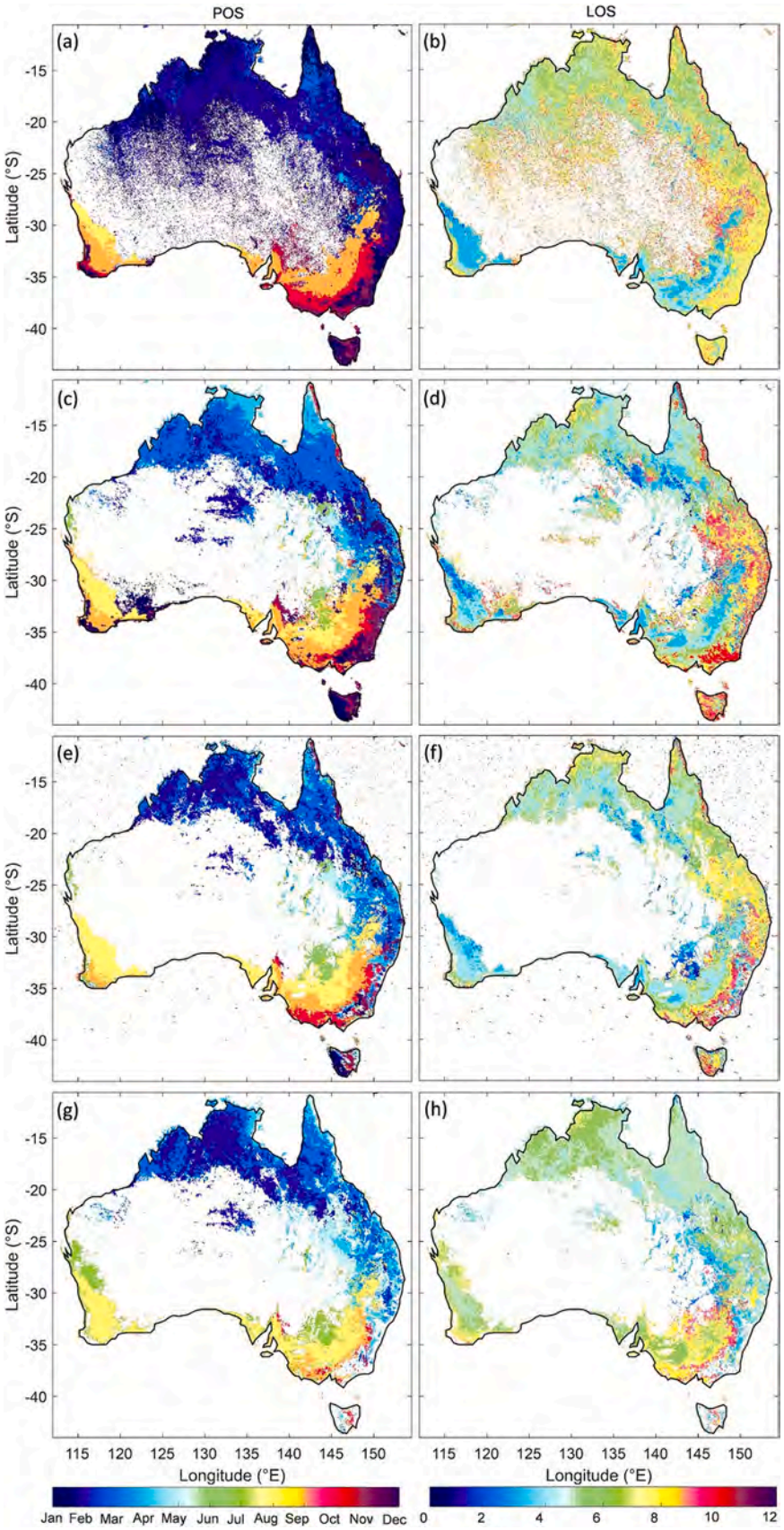

Fig. 6. Spatial distributions of TROPOMI SIF greenness proxies-extracted phenology months (i.e., the start of growing season (POS), the length of growing season (LOS)) over Australia from 2019–2022. **(a-b),** SIF-extracted POS and LOS; **(c-d),** LAI-extracted POS and LOS; **(e-f),** NIRv-extracted POS and LOS; **(g-h),** f_veg-extracted POS and LOS.

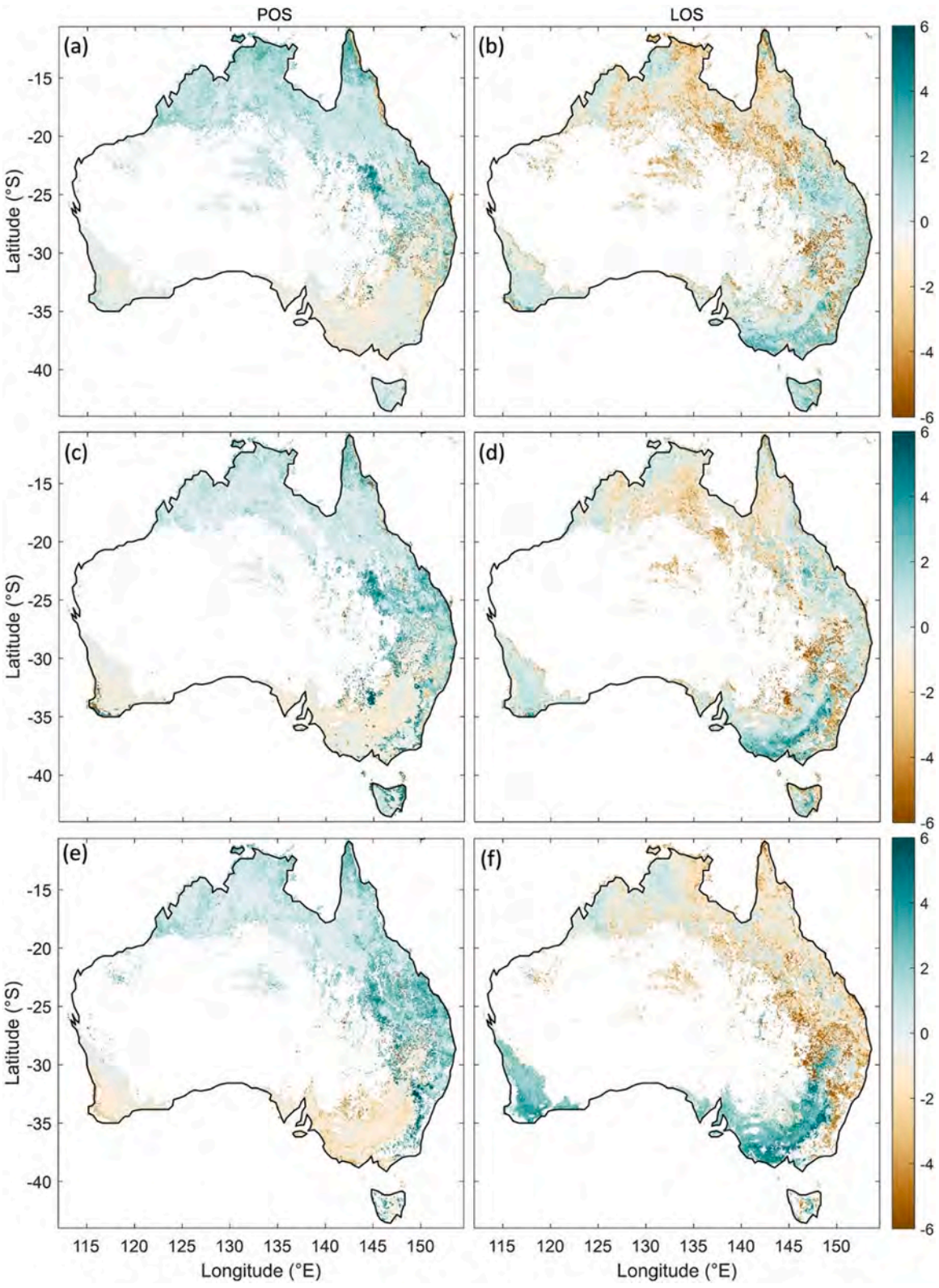

Fig. 7. Difference between TROPOMI SIF and greenness proxies-based phenology over Australia. **(a-b),** Difference between LAI-extracted and SIF-extracted POS and LOS; **(c-d),** Difference between NIRv-extracted and SIF-extracted POS and LOS; **(e-f),** Difference between f_veg-extracted and SIF-extracted POS and LOS. In **(a, c, e),** green areas indicate that POS derived from greenness proxies occurs later while POS derived from SIF occurs earlier, whereas brown areas indicate that greenness proxy-based POS occurs earlier and SIF-based POS occurs later. In **(b, d, f),** green areas indicate that greenness proxy-based LOS is longer while SIF-based LOS is shorter, whereas brown areas indicate that greenness proxy-based LOS is shorter and SIF-based LOS is longer.

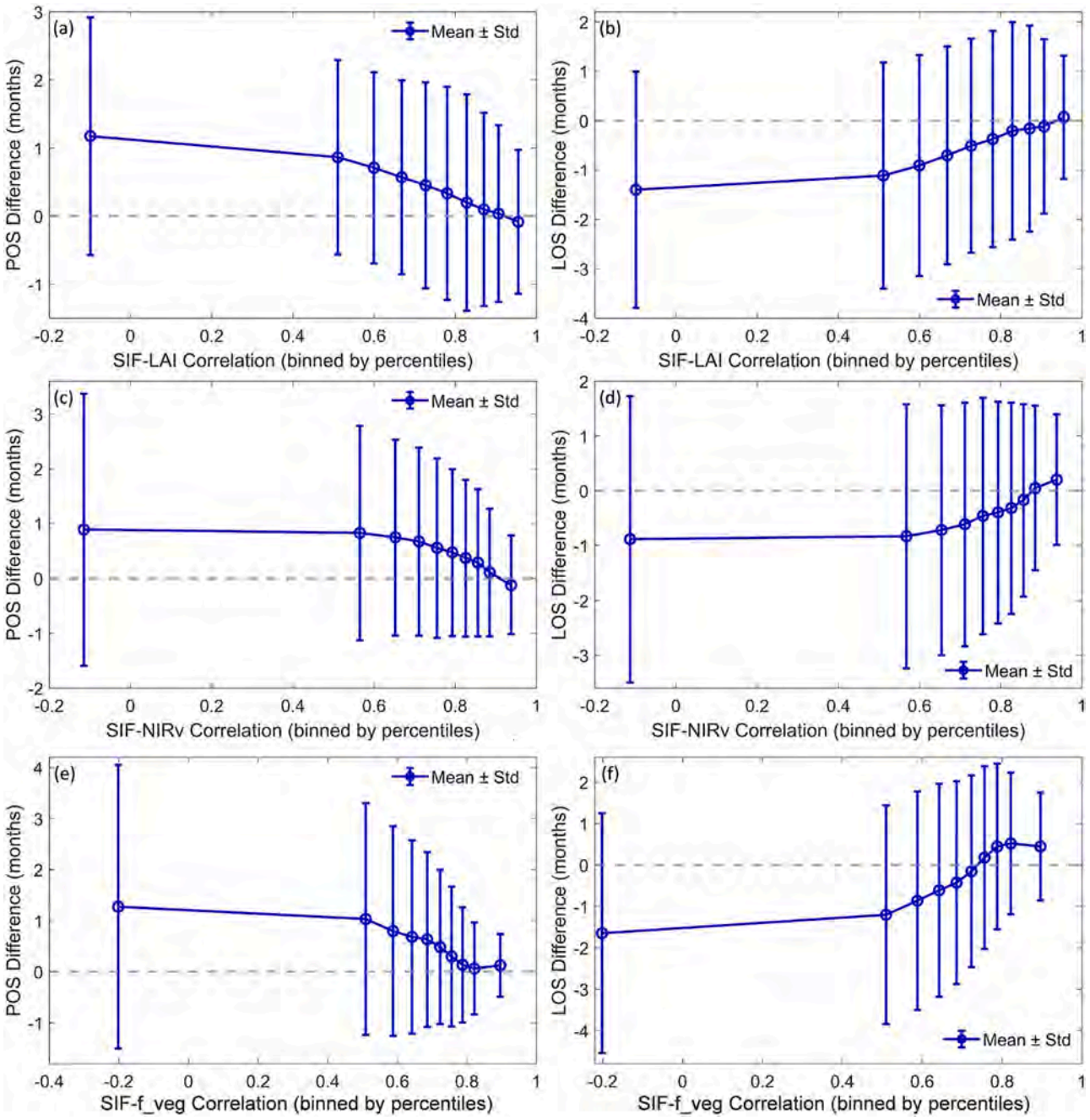

Fig. 8. Response of phenological differences along the gradients of SIF-greenness proxies' correlations. Phenological metrics include peak of growing season (POS) and length of season (LOS). **(a-b)**, Relationship between SIF-LAI correlation and POS and LOS differences; **(c-d),** Relationship between SIF-NIRv correlation and POS and LOS differences; **(e-f)**, Relationship between SIF-f_veg correlation and POS and LOS differences. Blue solid lines represent the mean values for each bin, with error bars indicating standard deviation (std). Gray dashed lines indicate zero reference.

stronger LAI–SIF coupling, this difference approached zero, and in highly coupled regions, LAI–derived LOS even became slightly longer than SIF-derived LOS (Fig. 8b). In addition, NIRv and f_veg exhibited similar trends (Fig. 8d, F), with a clear tendency for greenness-based LOS to exceed photosynthetic LOS in highly coupled regions. To further assess the robustness of the observed phenological patterns (Fig. 8), we repeated the analysis using a relaxed filtering threshold, where only pixels with amplitudes below 0.5 × the national median were excluded. The overall patterns remained broadly consistent (Figs. S10 and S11), suggesting that the results are robust to the filtering strategy.

Overall, our results clearly demonstrate a directional shift in ecosystem-level phenological responses under different levels of greenness–photosynthesis coupling, transitioning from a pattern of 'shorter greenness phenology' to 'longer greenness phenology'.

4. Discussion

This study examined vegetation structure–function coupling across Australia and its implications for differences between greenness- and SIF-derived phenology. TROPOMI SIF effectively captured GPP variability across diverse ecosystems in Australia. Compared to sparse canopies, SIF more closely tracks GPP variability in dense forest and woodland ecosystems (Fig. 1e, i). This can be attributed to the dominant contribution of sunlit upper leaves in dense canopies, which absorb a larger fraction of incoming radiation and thus govern both canopy SIF

and GPP (Yang et al., 2021). In contrast, in sparse canopies, increased sub-pixel heterogeneity and mixed-surface effects can reduce the representativeness of canopy-level SIF signals and weaken their relationship with GPP (Lu et al., 2020).

Our results suggest that the relationship between vegetation photosynthesis and greenness exhibited significant spatial heterogeneity across different climatic and vegetation zones in Australia. In semi-arid regions dominated by herbaceous vegetation, such as grasslands and croplands, canopy greenness was tightly coupled with photosynthetic dynamics. In contrast, in dense forests in humid regions, greenness proxies often become "decoupled" from SIF signals (Fig. 2), which may arise from trade-offs between leaf quantity and photosynthetic capacity (Hu et al., 2022), together with carbon allocation processes and associated temporal lags between carbon uptake and structural development (Griebel et al., 2017). This is consistent with previous study of Restrepo-Coupe et al. (2016), who integrated EC flux tower data with satellite-derived measures of greenness to reveal that, in Australia, photosynthetic activity does not exhibit significant relationships with satellite-derived greenness in relatively aseasonal ecosystems such as evergreen wet sclerophyll forests. In contrast, in ecosystems characterized by strong phenological dynamics (e.g., tropical savannas), flux tower-derived photosynthetic activity is effectively represented by greenness indices. Moreover, numerous studies have reported similar decoupling phenomena between vegetation structure and ecosystem function in humid forest ecosystems, especially in evergreen broadleaf forests (Tang et al., 2024; Hu et al., 2022; Zhang and Peñuelas, 2023). These findings imply that when evaluating carbon uptake dynamics across Australian ecosystems, it is insufficient to rely only on greenness-based structural remote sensing products. Instead, it is necessary to integrate multi-source remote sensing data that capture both structural and physiological changes, thereby reducing potential assessment biases and improving the accuracy of ecosystem functional dynamics.

We further found that the coupling between vegetation greenness and photosynthesis varied systematically along gradients of woody-fraction cover and aridity (Fig. 3). This can be ascribed to potential processes arising from fundamental differences in functional traits and adaptation strategies across ecosystems. In grassland-dominated ecosystems, the vegetation typically features shallow root systems and short leaf lifespans, with an ecological adaptation strategy that prioritizes rapid responses to environmental changes. This is achieved through adjustments in biomass allocation (such as the root-to-shoot ratio) to swiftly adapt variations in water availability (Canadell et al., 1996; Ma et al., 2018). Consequently, this may lead to a tight coupling between greenness and photosynthetic productivity. By contrast, in humid, woody ecosystems, root stratification and diverse community composition enable access to multi-layer water sources and the accumulation of substantial non-structural carbohydrate reserves (Saiki et al., 2017; Trugman et al., 2018; Tang et al., 2024). Meanwhile, under the combined effects of conservative stomatal regulation and hydraulic strategies (Xue et al., 2024), photosynthetic activity may significantly decline even when canopy greenness remains relatively stable, resulting in a structural–functional decoupling. These findings underscore the important role of vegetation composition and environmental factors in regulating the relationship between greenness and photosynthesis, highlighting the necessity of integrating multi-source remote sensing indicators that are sensitive to vegetation structure and physiological traits.

Another key finding of this study is the significant regulatory effect of water stress on the coupling between vegetation greenness and photosynthesis (Fig. 4, Fig. S6-8). Under extreme drought conditions (e.g., high VPD $>$ 70th percentile, low SMC $<$ 20th percentile), we observed a notable strengthening of the coupling between photosynthesis and vegetation structure, whereas decoupling occurred to varying degrees under wetter conditions (Fig. 4). A similar pattern was also reported by Li et al. (2024), who demonstrated that NDVI–GPP coupling strength was much higher in semi-arid regions compared to humid regions. Likewise, Jiao et al. (2020) showed that during the 1997–2009 Australian drought, structural–functional coupling strengthened, with croplands and grasslands exhibiting both the highest drought sensitivity and the strongest photosynthesis–structure coupling, which is consistent with our results in Figs. S6a, S7a, and S8a.

Sensitivity analyses further revealed that the SIF–greenness coupling showed contrasting dominant controls consistent with the physical nature of each proxy. LAI–SIF coupling was mainly influenced by soil moisture and vegetation structure, reflecting the importance of canopy configuration and soil water availability (Fig. 5a). Although LAI is indirectly related to absorbed photosynthetically active radiation (APAR) through its effect on light interception (Myneni et al., 2002), this relationship tends to saturate under dense canopies, thereby weakening the sensitivity of the coupling to radiation. NIRv, a canopy structure–related near-infrared reflectance of vegetation (Badgley et al., 2017), exhibited SIF coupling largely determined by vegetation compositional differences (Fig. 5b), consistent with its sensitivity to canopy structure and light energy absorption capacity. In contrast, for f_veg, which is linked to the fraction of photosynthetically active radiation absorbed by the canopy, the coupling with SIF was mainly driven by radiation (Fig. 5c). This highlights the importance of considering the distinct biophysical meanings of different greenness indicators when interpreting or modeling their relationships with photosynthetic activity.

From the perspective of carbon cycle modeling, satellite-derived greenness indices are widely used to constrain or improve DGVM simulations of phenology and productivity (Schürmann et al., 2016; Forkel et al., 2019). However, these models often exhibit systematic biases in phenological characterization, particularly in ecosystems where vegetation structure and function are asynchronous, leading to potential over-or underestimation of the LOS (Murray-Tortarolo et al., 2013; Song et al., 2021). Such phenological misrepresentations can produce cascading effects on carbon cycle simulations, ultimately affecting estimates of seasonal carbon balance (Norton et al., 2023; Chen et al., 2015; Haynes et al., 2019). A single phenology parameterization is unlikely to be universal across all ecosystems (Richardson et al., 2013), whereas SIF can more accurately represent the actual photosynthetic period, making it critical for improving parameterizations in terrestrial biosphere models (Zheng et al., 2023). In line with our findings, as the greenness–SIF coupling degree increased, phenological differences exhibited a systematic shift from “shorter greenness-based growing seasons” to “longer greenness-based seasons” (Fig. 8). This suggests that the period of greenness does not necessarily equate to a proportional duration of carbon uptake, and caution should be exercised when directly using greenness-derived phenology as a proxy for carbon sink phenology.

The systematic shift (Fig. 8) reflects the underlying spatial transition from weakly coupled, structurally complex systems in humid regions to strongly coupled, water-limited ecosystems in semi-arid regions. In semi-arid grasslands and croplands, vegetation dynamics are primarily controlled by water availability, with both canopy greenness and photosynthetic activity responding rapidly to precipitation variability, resulting in closely coupled seasonal dynamics (Huxman et al., 2004). In contrast, in humid forest and woodland ecosystems, high and persistent leaf area introduces structural inertia, allowing canopy greenness to remain relatively stable even when photosynthesis becomes constrained by environmental factors such as VPD or radiation (Jones et al., 2012; Yu et al., 2026). The muted seasonal amplitude and structural inertia of canopy greenness can obscure phenological transitions and reduce the detectability of seasonal signals, leading to a shortening of greenness-based LOS relative to SIF-derived phenology.

Moreover, our results highlight the potential of physiological phenology, as represented by SIF, to correct and constrain greenness-driven phenology metrics. The representativeness of greenness for the actual photosynthetic period varies across ecosystems, the SIF–greenness coupling strength can serve as a useful diagnostic constraint. In a

conceptual sense, future carbon cycle models could use coupling strength as a regional weighting factor, assigning greater confidence to greenness-based phenology where structure and function are tightly coupled, while introducing stronger physiological constraints where they are decoupled under different climate conditions and vegetation characteristics. This may help refine the framework of phenology modules, reduce seasonal biases caused by the decoupling between greenness and photosynthesis, and enhance model accuracy in simulating carbon dynamics (Peaucelle et al., 2019).

With increasing frequency of extreme climate events globally, ecosystems are likely to experience more frequent water stress, thereby possibly amplifying the uncertainties associated with traditional greenness-based methods for estimating GPP and phenology (Li et al., 2023; Liu et al., 2025). Our study offers a new perspective and scientific basis for improving carbon cycle modeling: it underscores the widespread occurrence of greenness–photosynthesis decoupling across ecosystems and climates, advances a theoretical understanding of phenological dynamics under conditions of vegetation structure–function asynchrony, and provides a practical framework for parameterizing and structurally optimizing terrestrial biosphere models. These contributions create opportunities to enhance future predictions of ecosystem carbon budgets and support more robust monitoring strategies in the future.

However, it is noteworthy that although SIF is considered a reliable proxy for plant photosynthesis, this relationship may weaken under certain conditions. The reduction in fluorescence and photochemical efficiencies during short periods of water stress do not have the same magnitude (Van der Tol et al., 2014; Marrs et al., 2020). Moreover, there is no consensus yet on how significantly these limited changes affect the SIF–GPP relationship at seasonal scales (Zhang et al., 2023b). Additionally, canopy structure and sun-sensor geometry can also affect the SIF–photosynthesis relationship (Zhang and Zhang, 2023). Therefore, more detailed analyses are needed to accurately leverage remotely sensed SIF for the retrieval of photosynthetic phenology. It is also worth noting that greenness proxies, such as LAI and NIRv, are subject to inherent limitations. LAI tends to saturate in high biomass regions, thereby limiting its sensitivity to variations in photosynthesis (Myneni et al., 2002). Similarly, NIRv integrates both structural and radiative components and can be influenced by canopy architecture and observation geometry (Hase et al., 2022). These inherent deviations may contribute to the observed inconsistencies between greenness proxies and SIF. Another limitation of this study is the relatively short observation window (2019–2022), which may not fully capture the cumulative effects of long-term climate variability and extreme events on vegetation phenological dynamics. Among currently available satellite-based SIF products, the TROPOMI SIF dataset used in this study provides a unique balance of high spatial resolution, continuous spatial sampling, and near-daily revisit frequency, although its temporal coverage is relatively short. In contrast, reconstructed SIF products (e.g., GOSIF) are typically derived from machine learning or statistical models that integrate reflectance and climate variables, rather than direct satellite retrievals. While these products provide valuable long-term information, they may introduce additional uncertainties associated with model structure, training data, and underlying assumptions (Shekhar et al., 2022). Future work should integrate longer time series from emerging global SIF observations and multi-source datasets to better characterize long-term trends and interannual variability in functional phenology (Kraft et al., 2013; Gamon et al., 2016; Shekhar et al., 2022).

5. Conclusion

By systematically comparing greenness indices with SIF across Australia, this study reveals how the greenness–photosynthesis coupling varies among ecosystems and how photosynthetic phenology diverges from greenness phenology. We find tight coupling in semi-arid, herbaceous systems but pronounced decoupling in humid forests, with coupling strength closely regulated by vegetation composition and water availability. Sensitivity analyses further revealed that the SIF–-greenness coupling is shaped by distinct environmental and structural controls across proxies, reflecting their differing roles in linking vegetation structure to photosynthetic function. Phenological differences between SIF- and greenness-derived metrics (e.g., POS, LOS) vary systematically with the strength of greenness–SIF coupling. Looking forward, future research integrating longer-term global SIF data and multi-source merged products will help systematically capture long-term trends and interannual variability in photosynthetic phenology, offering new opportunities to improve the parameterization of carbon cycle models and enhance ecosystem functional assessment under climate change.

CRediT authorship contribution statement

Jinru Xue: Writing – review & editing, Writing – original draft, Visualization, Software, Methodology, Investigation, Formal analysis, Data curation, Conceptualization. **Luigi J. Renzullo:** Writing – review & editing, Resources, Methodology, Funding acquisition, Data curation, Conceptualization. **Alfredo Huete:** Writing – review & editing, Supervision, Resources, Project administration, Investigation, Funding acquisition.

Declaration of competing interest

The authors declare that they have no known competing financial interests or personal relationships that could have appeared to influence the work reported in this paper.

Acknowledgments

This work was supported by the Bureau of Meteorology through the project JULES Phenology for Australia (3888-2023-24).

Supplementary materials

Supplementary material associated with this article can be found, in the online version, at doi:10.1016/j.agrformet.2026.111253.

Data availability

Data will be made available on request.

References

Badgley, G., Field, C.B., Berry, J.A., 2017. Canopy near-infrared reflectance and terrestrial photosynthesis. Sci. Adv. 3 (3), e1602244.
Baldocchi, D., et al., 2001. FLUXNET: a new tool to study the temporal and spatial variability of ecosystem-scale carbon dioxide, water vapor, and energy flux densities. Bull. Am. Meteorol. soc. 82 (11), 2415–2434.
Bennett, A.C., Knauer, J., Bennett, L.T., Haverd, V., Arndt, S.K., 2024. Variable influence of photosynthetic thermal acclimation on future carbon uptake in Australian wooded ecosystems under climate change. Glob. Chang. Biol. 30 (1), e17021.
Beringer, J., et al., 2022. Bridge to the future: important lessons from 20 years of ecosystem observations made by the OzFlux network. Glob. Chang. Biol. 28 (11), 3489–3514.
Cai, L., et al., 2023. Global models and predictions of plant diversity based on advanced machine learning techniques. New Phytol. 237 (4), 1432–1445.
Camps-Valls, G., et al., 2021. A unified vegetation index for quantifying the terrestrial biosphere. Sci. Adv. 7 (9), eabc7447.
Canadell, J., et al., 1996. Maximum rooting depth of vegetation types at the global scale. Oecologia 108 (4), 583–595.
Carlson, T.N., Ripley, D.A., 1997. On the relation between NDVI, fractional vegetation cover, and leaf area index. Remote Sens. Env. 62 (3), 241–252.
Chang, Q., et al., 2019. Assessing consistency of spring phenology of snow-covered forests as estimated by vegetation indices, gross primary production, and solar-induced chlorophyll fluorescence. Agric. Meteorol. 275, 305–316.
Chen, M., Griffis, T.J., Baker, J., Wood, J.D., Xiao, K., 2015. Simulating crop phenology in the Community Land Model and its impact on energy and carbon fluxes. J. Geophys. Res.: Biogeosci. 120 (2), 310–325.

Chen, A., Meng, F., Mao, J., Ricciuto, D., Knapp, A.K., 2022. Photosynthesis phenology, as defined by solar-induced chlorophyll fluorescence, is overestimated by vegetation indices in the extratropical Northern Hemisphere. Agric. Meteorol. 323, 109027.
Didan, K., Munoz, A.B., Solano, R., Huete, A., 2015. MODIS vegetation index user's guide (MOD13 series). Univ. Ariz.: Veg. Index Phenol. Lab 35, 2–33.
Donohue, R.J., Renzullo, L.J., 2025. An assessment of the accuracy of satellite-derived woody and grass foliage cover estimates for Australia. Aust. J. Bot. 73 (2).
Dubayah, R., et al., 2020. The Global Ecosystem Dynamics Investigation: high-resolution laser ranging of the Earth's forests and topography. Sci. Remote Sens. 1, 100002.
Forkel, M., et al., 2019. Constraining modelled global vegetation dynamics and carbon turnover using multiple satellite observations. Sci. Rep. 9 (1), 18757.
Fu, Z., et al., 2022. Atmospheric dryness reduces photosynthesis along a large range of soil water deficits. Nat. Commun. 13, 989.
Gamon, J.A., et al., 2016. A remotely sensed pigment index reveals photosynthetic phenology in evergreen conifers. Proc. Natl. Acad. Sci. 113 (46), 13087–13092.
Griebel, A., Bennett, L.T., Arndt, S.K., 2017. Evergreen and ever growing–Stem and canopy growth dynamics of a temperate eucalypt forest. For. Ecol. Manage. 389, 417–426.
Gu, L., Han, J., Wood, J.D., Chang, C.Y.Y., Sun, Y., 2019. Sun-induced chl fluorescence and its importance for biophysical modeling of photosynthesis based on light reactions. New Phytol. 223 (3), 1179–1191.
Guanter, L., et al., 2014. Global and time-resolved monitoring of crop photosynthesis with chlorophyll fluorescence. Proc. Natl. Acad. Sci. 111 (14), E1327–E1333.
Guanter, L., et al., 2021. The TROPOSIF global sun-induced fluorescence dataset from the Sentinel-5P TROPOMI mission. Earth Syst. Sci. Data 13 (11), 5423–5440.
Harris, R.M., et al., 2018. Biological responses to the press and pulse of climate trends and extreme events. Nat. Clim. Chang. 8 (7), 579–587.
Hase, N., et al., 2022. Identifying the main drivers of the seasonal decline of near-infrared reflectance of a temperate deciduous forest. Agric Meteorol. 313, 108746.
Haynes, K.D., et al., 2019. Representing grasslands using dynamic prognostic phenology based on biological growth stages: part 2. Carbon cycling. J. Adv. Model. Earth Syst. 11 (12), 4440–4465.
Hoerl, A.E., Kannard, R.W., Baldwin, K.F., 1975. Ridge regression: some simulations. Commun. Stat.-Theory Methods 4 (2), 105–123.
Hu, Z., et al., 2022. Decoupling of greenness and gross primary productivity as aridity decreases. Remote Sens. Env. 279, 113120.
Huxman, T.E., et al., 2004. Precipitation pulses and carbon fluxes in semiarid and arid ecosystems. Oecologia 141 (2), 254–268.
Isaac, P., et al., 2017. OzFlux data: network integration from collection to curation. Biogeosciences 14 (12), 2903–2928.
Jiao, T., Williams, C.A., Rogan, J., De Kauwe, M.G., Medlyn, B.E., 2020. Drought impacts on Australian vegetation during the millennium drought measured with multisource spaceborne remote sensing. J. Geophys. Res.: Biogeosci. 125 (2), e2019JG005145.
Jin, H., et al., 2023. Higher vegetation sensitivity to meteorological drought in autumn than spring across European biomes. Commun. Earth Environ. 4 (1), 299.
Jones, M.O., Kimball, J.S., Jones, L.A., McDonald, K.C., 2012. Satellite passive microwave detection of North America start of season. Remote Sens Env. 123, 324–333.
Kong, D., Zhang, Y., Wang, D., Chen, J., Gu, X., 2020. Photoperiod explains the asynchronization between vegetation carbon phenology and vegetation greenness phenology. J. Geophys. Res.: Biogeosci. 125 (8), e2020JG005636.
Kraft, S., et al., 2013. FLORIS: phase A status of the fluorescence imaging spectrometer of the Earth Explorer mission candidate FLEX, Sensors, Systems, and Next-Generation Satellites XVII. SPIE 154–165.
Lang, N., Jetz, W., Schindler, K. and Wegner, J.D., 2022. A high-resolution canopy height model of the Earth. arXiv preprint arXiv:2204.08322.
Li, W., et al., 2023. Widespread and complex drought effects on vegetation physiology inferred from space. Nat. Commun. 14 (1), 4640.
Li, Y., Yuan, X., Zheng, L., Zhang, W., Zhang, Y., 2024. Decoupling and insensitivity of greenness and gross primary productivity across aridity gradients in China. Remote Sens. 16 (22), 4234.
Liu, Z., et al., 2024. A SIF-based approach for quantifying canopy photosynthesis by simulating the fraction of open PSII reaction centers (qL). Remote Sens Env. 305, 114111.
Liu, M., et al., 2025. Diverging responses of terrestrial ecosystems to water stress after disturbances. Nat. Clim. Chang. 15 (1), 73–79.
Lu, X., Liu, Z., Zhao, F., Tang, J., 2020. Comparison of total emitted solar-induced chlorophyll fluorescence (SIF) and top-of-canopy (TOC) SIF in estimating photosynthesis. Remote Sens. Env. 251, 112083.
Ma, Z., et al., 2018. Evolutionary history resolves global organization of root functional traits. Nature 555 (7694), 94–97.
Marrs, J., et al., 2020. Solar-induced fluorescence does not track photosynthetic carbon assimilation following induced stomatal closure. Geophys. Res. Lett. 47 (15), e2020GL087956.
Muñoz-Sabater, J., et al., 2021. ERA5-Land: a state-of-the-art global reanalysis dataset for land applications. Earth Syst. Sci. Data 13 (9), 4349–4383.
Muraoka, H., et al., 2013. Spectral vegetation indices as the indicator of canopy photosynthetic productivity in a deciduous broadleaf forest. J. Plant Ecol. 6 (5), 393–407.
Murray-Tortarolo, G., et al., 2013. Evaluation of land surface models in reproducing satellite-derived LAI over the high-latitude Northern Hemisphere. Part I: uncoupled DGVMs. Remote Sens. 5 (10), 4819–4838.
Myneni, R., Williams, D., 1994. On the relationship between FAPAR and NDVI. Remote Sens. Env. 49 (3), 200–211.
Myneni, R.B., et al., 2002. Global products of vegetation leaf area and fraction absorbed PAR from year one of MODIS data. Remote Sens. Env. 83 (1–2), 214–231.
Myneni, R., Knyazikhin, Y. and Park, T., 2015. MCD15A3H MODIS-/Terra+ Aqua Leaf area index/FPAR 4-day L4 Global 500m SIN grid V006, NASA EOSDIS Land Processes DAAC [data set].
Norton, A.J., et al., 2023. Improved process representation of leaf phenology significantly shifts climate sensitivity of ecosystem carbon balance. Biogeosciencess 20 (12), 2455–2484.
Peaucelle, M., et al., 2019. Spatial variance of spring phenology in temperate deciduous forests is constrained by background climatic conditions. Nat. Commun. 10 (1), 5388.
Piao, S., et al., 2019. Plant phenology and global climate change: current progresses and challenges. Glob. Chang. Biol. 25 (6), 1922–1940.
Porcar-Castell, A., et al., 2014. Linking chlorophyll a fluorescence to photosynthesis for remote sensing applications: mechanisms and challenges. J. Exp. Bot. 65 (15), 4065–4095.
Potapov, P., et al., 2021. Mapping global forest canopy height through integration of GEDI and Landsat data. Remote Sens. Env. 253, 112165.
Restrepo-Coupe, N., et al., 2016. MODIS vegetation products as proxies of photosynthetic potential along a gradient of meteorologically and biologically driven ecosystem productivity. Biogeosciences 13 (19), 5587–5608.
Richardson, A.D., et al., 2013. Climate change, phenology, and phenological control of vegetation feedbacks to the climate system. Agric. Meteorol. 169, 156–173.
Saiki, S.-T., Ishida, A., Yoshimura, K., Yazaki, K., 2017. Physiological mechanisms of drought-induced tree die-off in relation to carbon, hydraulic and respiratory stress in a drought-tolerant woody plant. Sci. Rep. 7 (1), 2995.
Saleska, S.R., et al., 2016. Dry-season greening of Amazon forests. Nature 531 (7594), E4–E5.
Schürmann, G.J., et al., 2016. Constraining a land-surface model with multiple observations by application of the MPI-Carbon Cycle Data Assimilation System V1. 0. Geosci. Model. Dev. 9 (9), 2999–3026.
Shan, N., et al., 2021. A model for estimating transpiration from remotely sensed solar-induced chlorophyll fluorescence. Remote Sens. Env. 252, 112134.
Shekhar, A., Buchmann, N., Gharun, M., 2022. How well do recently reconstructed solar-induced fluorescence datasets model gross primary productivity? Remote Sens. Env. 283, 113282.
Song, X., Wang, D.-Y., Li, F., Zeng, X.-D., 2021. Evaluating the performance of CMIP6 earth system models in simulating global vegetation structure and distribution. Adv. Clim. Change Res. 12 (4), 584–595.
Tang, J., Niu, B., Hu, Z., Zhang, X., 2024. Increasing susceptibility and shortening response time of vegetation productivity to drought from 2001 to 2021. Agric. Meteorol. 352, 110025.
Trugman, A., et al., 2018. Tree carbon allocation explains forest drought-kill and recovery patterns. Ecol. Lett. 21 (10), 1552–1560.
Van der Tol, C., Berry, J., Campbell, P., Rascher, U., 2014. Models of fluorescence and photosynthesis for interpreting measurements of solar-induced chlorophyll fluorescence. J. Geophys. Res.: Biogeosci. 119 (12), 2312–2327.
Vermote, E., 2015. MOD09A1 MODIS/Terra Surface Reflectance 8-Day L3 Global 500m SIN Grid V006. In: NASA EOSDIS Land Processes DAAC. https://doi.org/10.5067/MODIS/MOD09A1.006.
Walther, S., et al., 2016. Satellite chlorophyll fluorescence measurements reveal large-scale decoupling of photosynthesis and greenness dynamics in boreal evergreen forests. Glob. Chang. Biol. 22 (9), 2979–2996.
Walther, S., et al., 2019. Satellite observations of the contrasting response of trees and grasses to variations in water availability. Geophys. Res. Lett. 46 (3), 1429–1440.
Wang, X., et al., 2020. Globally consistent patterns of asynchrony in vegetation phenology derived from optical, microwave, and fluorescence satellite data. J. Geophys Res.: Biogeosci. 125 (7), e2020JG005732.
Wu, J., et al., 2016. Leaf development and demography explain photosynthetic seasonality in Amazon evergreen forests. Science 351 (6276), 972–976.
Wu, C., et al., 2017. Land surface phenology derived from normalized difference vegetation index (NDVI) at global FLUXNET sites. Agric. Meteorol. 233, 171–182.
Xue, J., Huete, A., Liu, Z., Wang, Y., Lu, X., 2024. Estimation of global ecosystem isohydricity from solar-induced chlorophyll fluorescence and meteorological datasets. Remote Sens. Env. 307, 114168.
Yang, P., Van der Tol, C., Campbell, P.K., Middleton, E.M., 2021. Unraveling the physical and physiological basis for the solar-induced chlorophyll fluorescence and photosynthesis relationship using continuous leaf and canopy measurements of a corn crop. Biogeosciences 18 (2), 441–465.
Yu, H., Mo, Z., Tan, T., Qiu, L., Guo, L., 2026. Earlier spring onset and autumn warming increase the discrepancy between leaf coloration and photosynthetic cessation. Commun. Earth Environ. 7.
Zhang, Y., Peñuelas, J., 2023. Combining solar-induced chlorophyll fluorescence and optical vegetation indices to better understand plant phenological responses to global change. J. Remote Sens. 3, 0085.
Zhang, Z., Zhang, Y., 2023. Solar angle matters: diurnal pattern of solar-induced chlorophyll fluorescence from OCO-3 and TROPOMI. Remote Sens. Env. 285, 113380.
Zhang, Y., et al., 2016. Canopy and physiological controls of GPP during drought and heat wave. Geophys. Res. Lett. 43 (7), 3325–3333.
Zhang, Y., Parazoo, N.C., Williams, A.P., Zhou, S., Gentine, P., 2020. Large and projected strengthening moisture limitation on end-of-season photosynthesis. Proc. Natl. Acad. Sci. 117 (17), 9216–9222.
Zhang, J., et al., 2022. NIRv and SIF better estimate phenology than NDVI and EVI: effects of spring and autumn phenology on ecosystem production of planted forests. Agric. Meteorol. 315, 108819.

Zhang, J., et al., 2023a. Solar-induced chlorophyll fluorescence captures photosynthetic phenology better than traditional vegetation indices. ISPRS J. Photogramm. Remote Sens. 203, 183–198.
Zhang, Y., et al., 2023b. Satellite solar-induced chlorophyll fluorescence tracks physiological drought stress development during 2020 southwest US drought. Glob. Chang. Biol. 29 (12), 3395–3408.
Zheng, C., et al., 2023. Combination of vegetation indices and SIF can better track phenological metrics and gross primary production. J. Geophys. Res.: Biogeosci. 128 (7), e2022JG007315.
Zhou, L., et al., 2022. Land surface phenology detections from multi-source remote sensing indices capturing canopy photosynthesis phenology across major land cover types in the Northern Hemisphere. Ecol. Indic. 135, 108579.
Zomer, R.J., Xu, J., Trabucco, A., 2022. Version 3 of the Global Aridity Index and Potential Evapotranspiration Database. Sci. Data 9 (1), 409.